Local stress models do not predict observed crevasse patterns at Greenland's marine terminating glaciers

Ellyn M. Enderlin[1], Timothy C. Bartholomaus[2]

[1]Department of Geosciences, Boise State University, Boise, Idaho, 83725, USA
[2]Department of Geological Sciences, University of Idaho, Moscow, Idaho, 83844, USA

Correspondence to: Ellyn M. Enderlin (ellynenderlin@boisestate.edu)

Abstract. Crevasses are affected by and affect both stresses and surface mass balance of glaciers. These effects are brought on through potentially important controls on meltwater routing, glacier viscosity, and iceberg calving, yet there are few direct observations of crevasse sizes and locations to inform our understanding of these interactions. Here we extract crevasse depth estimates from high-resolution surface elevation observations for 52,644 crevasses from 19 Greenland glaciers. We then compare our observed depths with those calculated using two popular models that assume crevasse depths are functions of local stresses: the Nye and linear elastic fracture mechanics (LEFM) formulations . We find that along-flow patterns in crevasse depths are unrelated to along-flow patterns in strain rates (and therefore stresses), but that cumulative strain rate is more predictive of crevasse depths. Both the Nye and LEFM approaches can be tuned to reproduce observed, average crevasse depths, but along-flow variations in observed and modeled crevasse depths remain uncorrelated. This leads us to conclude that neither model adequately captures the physics controlling crevasse evolution at fast-flowing glaciers. Our finding motivates us to question glacier and ice sheet change projections that rely on Nye or LEFM-based calving.

1 Introduction

The geometry and concentration of crevasses are both affected by and affect the stress state and surface mass balance of glaciers, ice shelves, and ice sheets (Colgan et al., 2016). Changes in crevasse geometry and concentration can arise as the result of long-term or rapid changes in stress state, serving as a valuable tool to infer the onset of kinematic change (Colgan et al., 2011; Trantow and Herzfeld, 2018). These changes can also influence the stress state. For example, changes in crevassing within lateral shear margins of Antarctic ice streams have the potential to dramatically alter the ability of ice streams to buttress flow from the interior, in turn exerting an important control on ice sheet stability (Borstad et al., 2016; Reese et al., 2018). The impoundment of surface meltwater runoff in crevasses can promote crevasse penetration and assist in the penetration of meltwater to the glacier bed (van der Veen, 1998; Stevens et al., 2015; Poinar et al., 2017), influencing the englacial and basal stress states. Crevasses also increase surface roughness, altering the incidence angle of solar radiation and turbulent energy fluxes, which in turn influence surface melt production (Pfeffer and Bretherton, 1987; Andreas, 2002; Hock, 2005; Cathles et al., 2011; Colgan et al., 2016).

These interactions between crevasses, stresses, and surface mass balance make crevasses particularly important components of terrestrial ice, particularly near the termini of the marine-terminating glaciers and ice streams draining Greenland and Antarctica. In Antarctica, observations and models indicate that the ice shelves fringing the continent are highly vulnerable to widespread crevasse hydrofracture in a warming climate (Pollard et al., 2015; Rott et al., 1996; Scambos et al., 2000, 2009). The influence of crevasses, and changes in crevassing over time due to atmospheric warming, are less clear for Arctic marine-terminating glaciers. Despite the abundance of crevasses throughout the marginal zone of the Greenland ice sheet, there are few observations of crevasse depths at Greenland's glaciers. However, the coincident increase in surface meltwater runoff and widespread retreat of glacier termini across Greenland (Carr et al., 2017; Howat and Eddy, 2011; Moon and Joughin, 2008) suggests that hydrofracture may exert a first-order control on calving (Benn et al., 2007a; Cook et al., 2014).

Since calving involves the mechanical detachment of ice from a glacier terminus, it has been assumed that calving occurs when and where surface crevasses penetrate the full ice thickness (Benn et al., 2007a). The penetration depth of crevasses has been traditionally modeled using either the linear elastics fracture mechanics (LEFM) or Nye formulations, which assume that crevasse depth is dictated by local longitudinal stresses. For a single crevasse, the LEFM formulation estimates the stress concentration at the crevasse tip as

$$K_I = F(\lambda) R_{xx} \sqrt{\pi d_{modeled}}, \quad (1)$$

where the modeled crevasse depth, $d_{modeled}$, is the maximum depth where the stress concentration is sufficient to overcome the fracture toughness of the ice (van der Veen, 1998). In Eqn. 1, R_{xx} is the full stress minus the lithostatic stress (estimated using strain rates) and $F(\lambda)$ is a geometric parameter that accounts for the non-linear increase in the stress intensity factor as a crevasse penetrates deeper into the glacier and the ratio of the crevasse depth to ice thickness, λ, increases (van der Veen, 1998). For closely-spaced crevasses, concentration of stresses at crevasse tips can be ignored and surface crevasse depths can be estimated using the Nye formulation (Nye, 1957), such that

$$d_{modeled} = \frac{2}{\rho_i g}\left(\frac{\dot{\varepsilon}_{xx} - \dot{\varepsilon}_{crit}}{A}\right)^{1/3} + \frac{\rho_w}{\rho_i} h_w \,, \quad (2)$$

where ρ_i and ρ_w are the densities of ice (917 kg m^{-3}) and water (1000 kg m^{-3}), g is gravitational acceleration (9.81 m s^{-2}), $\dot{\varepsilon}_{xx}$ is the longitudinal strain rate (yr^{-1}), $\dot{\varepsilon}_{crit}$ is the critical strain rate threshold for crevasse formation (yr^{-1}), A is the creep parameter describing ice viscosity (Pa^{-3} yr^{-1}), and h_w is the depth of water in crevasses. Neither formulation has been rigorously validated using crevasse depth observations, but data from Breiðamerkurjökull, Iceland, suggest that the LEFM formulation is more accurate than the Nye formulation when a priori information on crevasse geometries are available to constrain $F(\lambda)$ (Mottram and Benn, 2009).

Despite its potential over-estimation of crevasse depths (Mottram and Benn, 2009), the Nye formulation has been implemented in a number of numerical ice flow models as the terminus boundary condition (Cook et al., 2014; Nick et al., 2013; Vieli and Nick, 2011). The Nye formulation has been used in lieu of the LEFM formation because observations of dense crevasse fields

near glacier termini suggest considerable stress blunting occurs and the a priori information on crevasse geometries needed to tune the LEFM formulation are lacking. Using Eq. 2, the ice viscosity or water depth in crevasses can conceivably be tuned to drive changes in crevasse depth, so that the modeled terminus position change matches observations. The high sensitivity of simulated terminus positions to changes in water depth (Cook et al., 2012, 2014; Otero et al., 2017), however, lead us to question the appropriateness of this model. Furthermore, there is no assurance that the modeled crevasse depths reproduce observations or that the crevasse depth parameterization accounts for the primary control(s) on terminus change. Because model projections of dynamic mass loss may well be in error if driven by an inaccurate calving parameterization, increased confidence in dynamic mass loss projections drawing on these calving parameterizations requires validation of modeled crevasse depths.

Here we construct the first extensive record of crevasse depths for Greenland's fast-flowing outlet glaciers using airborne lidar and high-resolution digital elevation models from 2011-2018. We compare these observed crevasse depths with modeled crevasse depths derived from satellite-based velocity fields to assess the accuracy of modeled crevasse depths. Furthermore, we examine the likelihood that spatio-temporal variations in crevasse depth can explain observed variations in terminus position change and associated dynamic mass loss for Greenland's marine-terminating outlet glaciers. Although we focus on Greenland, our assessment of 19 glaciers spanning a wide range of geometries, climate regimes, and dynamic histories (Fig. 1a) increases the likelihood that our results are broadly applicable to glaciers throughout the Arctic.

2 Methods

2.1 Observed Crevasse Depths

Surface crevasses exist as fractures in ice that extend from glacier surfaces, generally as some sort of visible opening within a glacier, and continue down to the bottom of a fracture, to unbroken ice. While the full crevasse depth is unmeasurable from glacier surfaces, we assume here that the depth of the visible, near-surface void space is positively correlated with the full depth of the crevasse, which likely extends beyond the depth of the void space. We refer to the maximum, visibly open depth below the surface as the observed crevasse depth.

We construct time series of crevasse depths from flow-following lidar swaths acquired by NASA Operation IceBridge (OIB) and 2 m-resolution digital elevation models (DEMs) using a semi-automated approach that identifies crevasses from local elevation minima (Figs. 1b-e). We use lidar observations from the OIB ATM (Advanced Topographic Mapper), which has a vertical precision of better than 1cm and spatial sampling of one pulse every ~10 m^2 within its conical swath (https://nsidc.org/data/ilatm1b). Repeat April/May flow-following observations are available for all our study sites during the 2013-2018 period. Elevations were also extracted from 2 m-resolution DEMs produced by the Polar Geospatial Center as part

of the ArcticDEM program. The WorldView DEMs are less precise (3m vertical uncertainty (Noh and Howat, 2015)) but provided estimates of elevation throughout the 2011-2018 melt seasons. We used an average of ~4 lidar swaths and ~16 DEMs per glacier for our analysis.

Lidar swaths were overlain on cloud-free summer Landsat 8 images and swath centerlines were manually traced to the inland extents of visible crevassing. Using a moving window approach, shifted at ~1 m increments along the swath centerlines, we linearly interpolated the nearest elevation data, then identified crevasses using a filtering process described below and illustrated for Kong Oscar Gletsjer in Fig. 1. To identify crevasses, centerline elevations were first detrended over the ~500 m-wide moving window (Fig. 1b inset), then the local elevation minimum and maximum were extracted from each of three smaller windows centered on the detrended profile (Fig. 1b, gray shading). The process was repeated over the full profile length, resulting in the identification of local lows and highs for each elevation profile. The minimum elevation was identified from each grouping of contiguous low points, a similar procedure was used to define high points, and the remaining points were discarded (Fig. 1c). For each minimum, the closest neighboring down- and up-glacier maxima were used to define longitudinal crevasse widths (Fig. 1d). Potential collapsed seracs at the bottom of crevasses and small surface irregularities less than the vertical uncertainty of the DEMs were discarded.

The appropriate lengths for the detrending window and search windows to identify the local minima were determined through a comparison of manual and automated crevasse depth distributions (i.e., depths and their locations) from the most complete lidar profile for each glacier. Six detrending window sizes and two sets of search window sizes were tested, for a total of 12 test combinations, as outlined in Table S1. The range of possible detrending window sizes was constrained by the requirements that the window (1) spanned the largest crevasses (~200 m in width at Helheim Glacier) and (2) did not exceed the maximum half-wavelength of large-scale oscillations in surface elevation evident along the profiles (~800-1500m). For the search windows, we tested sizes that minimally spanned the maximum observed half-width of crevasses, but fully spanned the majority of crevasses: the median width ± 1.48 MAD (median of absolute deviation) of the 3264 manually-identified crevasses, which is analogous to the mean ± the standard deviation for normally-distributed data, was 19.2 ± 10.2 m and the maximum width was 184 m. The optimal window combination used for automated crevasse identification was the window combination that yielded the smallest number of falsely-identified crevasses (both false positives and false negatives) and the smallest depth misfit relative to the manually-extracted dataset. Optimal window sizes were glacier-dependent. The optimal detrending window sizes ranged from 350-800 m (9=350 m, 2=500 m, 3=550 m, 1=650 m, 4=800 m). The smaller search window sizes were considered optimal for all study sites except Helheim Glacier, which had the widest crevasses. For these optimal window sizes, the median false negative rate was 1.2% and the median false positive rate was 38.5% across all glaciers. In other words, the automated algorithm missed ~1% of manually-identified crevasses and identified ~38% more crevasses than the manual interpreter.

Given the off-nadir scan angle of the OIB lidar and the stereo imagery used to construct the DEMs, it is highly unlikely that the elevation observations penetrate to the bottom of the open portion of all crevasses. Therefore, following the approach of Liu et al. (2014), who used ICESat data to estimate crevasse depths across the Amery Ice Shelf, we estimated the depths of open crevasses using a V-shaped cross-sectional geometry. Based on the commonality of V-shaped crevasses in our elevation transects, we assumed that crevasses initially form with V shapes and negligible fracture extent beyond the bottom of these `V's. As stated above, further fracturing below the bottom of the V is possible, although we would then expect it to also open under the same extensional strain rates that open the V shapes above. Apparent deviations from an idealized V-shaped geometry are likely due to serac toppling, over-printing of new crevasses on previously damaged ice (Colgan et al., 2016), the presence of impounded meltwater, or occlusion of the lidar signal by the walls of the crevasse or ice debris in the crevasse. To estimate the true depth of the open portion of each crevasse, we linearly projected both crevasse walls to depth and identified their extrapolated point of intersection (Fig. 1e). For each elevation minimum and closest neighboring down- and up-glacier maxima, the crevasse walls were identified as contiguous regions with slopes within the typical range observed for manually-identified V-shaped crevasses in the window-calibration elevation profiles. Since there is no physical reason why the crevasse wall surface slopes should be normally distributed, we used the median ± 1.48 MAD to characterize the typical range. For normally distributed data, this formulation would be analogous to the mean ± standard deviation. For irregularly-shaped crevasses and for crevasses located where the rough glacier surface resulted in local elevation maxima several meters to tens of meters from the crevasse edge, this approach retracted the crevasse wall extents to correspond with slope breaks. If wall slopes were entirely outside of the typical range, there was no effect on the crevasse extents. We refer to the average elevation difference between the top and bottom of crevasses as the observed crevasse depths, and represent minimum estimates of the full penetration depth of ice fracture beneath crevasses.

We estimated uncertainties associated with (1) spatial resolution of the satellite-derived DEMs through comparison of same-day ATM profiles, (2) the automated approach for crevasse identification through comparisons with depths from manually-identified crevasses, and (3) crevasse depth extrapolation through comparisons between observed and extrapolated depths for V-shaped crevasses. All values presented are the median ± 1.48 MAD unless otherwise stated.

Although the precision of the lidar elevations is better than 1cm, the discrete sampling of the lidar may not be coincident with the location of the true crevasse bottom. Uncertainties associated with the lidar spatial sampling were quantified through a comparison of crevasse depths extracted from same-day up- and down-glacier swaths. The difference in crevasse depths between repeat swaths was -0.35 ± 2.5 m. We attribute the non-zero mean depth difference to slight differences in crevasse wall slopes between repeat observations. Uncertainties associated with the inclusion of the lower resolution WorldView DEM-derived depths were estimated through a comparison of same day lidar- and DEM-derived crevasse depths. We found that the DEM-derived depths were 1.0 m less than the lidar-derived depths, with a MAD of 2.5 m. A comparison of high-resolution and 2 m-resolution lidar-derived crevasse depths indicated the decrease in horizontal resolution of the DEMs accounted for

~1/3 of the DEM-derived depth bias. Since the potential biases were within the uncertainties in the datasets, we do not discuss them further. The lidar-derived depth uncertainty and the MAD from the lidar-DEM depth comparison were summed in quadrature to obtain a DEM-derived depth uncertainty of 3.0 m.

Uncertainties associated with automated crevasse depth estimation were quantified through a comparison of manually- and automatically-extracted crevasse depths. Automation uncertainties were minimized through the use of manual calibration datasets. Typical uncertainties introduced by the use of our automated approach were -0.3 ± 0.6 m, indicating that the automated approach slightly over-estimated crevasse depths due to differences in the manual versus automated identification of crevasse wall limits.

Our assumption of V-shaped crevasses was supported by observations of abundant V-shaped crevasses in every elevation profile examined here. For the V-shaped crevasses identified in the calibration profiles, the difference between the observed and extrapolated depths was <0.1 m on average. Examples of V-shaped crevasses can be found in Fig. 1 and scatterplots comparing observed and extrapolated depths for V-shaped and irregularly-shaped crevasses are shown in Fig. S1.

Overall, we estimate lidar-derived and DEM-derived depth uncertainties of 2.5 m and 4.4 m, respectively, with the tendency toward slight under-estimation of crevasse depths (1.0 m bias) when using DEMs. Automation results in a slight over-estimation (0.3 m) of crevasse depths due to differences in the manual and automated crevasse wall extents. The difference between observed and extrapolated crevasse depths for V-shaped crevasses is <0.1 m, indicating an excellent linear crevasse wall approximation and inconsequential bias associated with extrapolated depths (Fig. S1).

2.2 Modeled Crevasse Depths

Modeled crevasse depths were calculated using the (1) Nye formulation for densely-spaced crevasses and (2) LEFM formulation for an individual crevasse. Here we primarily focus on the Nye formulation given its more widespread use in calving parameterizations. For both formulations, crevasses are only expected under tension, with the deepest crevasses in locations with the highest longitudinal stresses and most viscous (i.e., colder and/or less damaged) ice. Neither formulation accounts for 'inheritance', meaning the crevasse depths are estimated as functions of the local, instantaneous, longitudinal stress without consideration of crevasse advection.

Strain rates were computed from NASA Making Earth System Data Records for Use in Research Environments (MEaSUREs) Interferometric Synthetic Aperture Radar velocities (https://nsidc.org/data/NSIDC-0481/versions/1). The temporal coverage of these approximately bi-weekly velocity fields varied widely between glaciers, with an average of 66 velocity maps per glacier and a maximum of 282 maps for Jakobshavn from 2011-2018. Spatial gradients in velocity were used to compute strain

rates in the native (polar stereographic) coordinate system, which were then rotated into flow-following coordinates. The creep parameter (A) is dependent on a number of variables, including ice temperature, crystal fabric development, and damage, but is poorly constrained by observations. Here, we approximated temperature-dependent spatial variations in the creep parameter as a linear function of latitude (Nick et al., 2013). Longitudinal strain rates were calculated over the full velocity domain then linearly interpolated to the swath centerlines.

For our initial estimates using the Nye model, what we term the 'minimal' model, we followed the approach of Mottram and Benn (2009) and assumed crevasses formed everywhere under tension (i.e., no critical strain rate threshold) and there was no water in crevasses (likely the case for spring OIB data). To improve model performance, we also tested several more complex versions of the model. We first estimated the critical strain rate for crevasse formation at each glacier as the maximum strain rate inland of the most up-glacier crevasse observation. To explore the potential contribution of the ice viscosity parameterization to the observed-modeled depth discrepancy, we assumed that the observed crevasse depths are accurate and constructed profiles of the deformation enhancement factor needed to minimize the misfit between observed and modeled crevasse depths. Similar to Borstad et al. (2016), we included a deformation enhancement factor, D, in these calculations as

$$d_{observed} = (1 - D)\left[\frac{2}{\rho_i g}\left(\frac{\dot{\varepsilon}_{xx}}{A}\right)^{1/3}\right]. \quad (3)$$

Substituting our initial modeled crevasse depths (i.e., Eq. (2) with $\dot{\varepsilon}_{crit} = 0$ and $h_w = 0$) in for the RHS term in brackets and rearranging to solve for the deformation enhancement factor, we obtained

$$D = \frac{d_{modeled} - d_{observed}}{d_{modeled}}. \quad (4)$$

Although similar to damage in Borstad et al. (2016), our deformation enhancement factor is a function of spatial variations in damage, ice temperature, and crystal fabric. A unique deformation factor can be identified at each crevasse location using Eq. (4). However, such detailed tuning is neither physically motivated nor practical for models, so we binned the data along-flow then parameterized deformation enhancement as a linear function of distance from the terminus using the binned data (Fig. S2). The deformation enhancement factors for the deepest crevasses over each 300 m bin, spanning from the terminus to the inland-most crevasse observation, were used in our parameterizations. Finally, we also used the inland-most deformation enhancement value to solve for modeled crevasse depths under the assumption of spatially uniform ice viscosity, then estimated impounded water depths from the misfit between the observed and modeled crevasse depths. Again, we sought a simple parameterization appropriate for use in numerical ice flow models: assuming that water depth varies with meltwater generation, we parameterized impounded water depth as linear function of surface elevation for each glacier (Fig. S3). For the damage and impounded water depth parameterizations, bin size did not influence along-flow patterns discussed below.

Although numerical ice flow models have relied on the Nye formulation to model crevasse depths, the previously-observed over-estimation of crevasse depths by the Nye formulation relative to both observations and the LEFM formulation (Mottram

and Benn, 2009) suggests there may be large differences in accuracy of the Nye and LEFM formulations. We solved for LEFM crevasse depths as the maximum depth where the stress intensity factor from Eq. (1) no longer exceeded the fracture toughness of ice, K_{IC}. In line with Mottram and Benn (2009), we used K_{IC} =50kPa m$^{1/2}$ as our best estimate and constrained uncertainty in this term using minimum and maximum values of 10kPa m$^{1/2}$ and 100kPa m$^{1/2}$, respectively. Longitudinal stress, σ_{xx}, was calculated from the measured strain rate tensors using

$$\sigma_{xx} = A^{-1/n} \dot{\varepsilon}_e^{(1-n)/n} \dot{\varepsilon}_{xx}, \quad (5)$$

where $\dot{\varepsilon}_e$ and $\dot{\varepsilon}_{xx}$ are the second invariant of the strain rate tensor (i.e., effective strain rate, assuming negligible vertical shear) and the longitudinal strain rate in the direction of ice flow, respectively, and n=3. The lithostatic stress was subtracted from σ_{xx} to estimate the longitudinal resistive stress, R_{xx}. Longitudinal resistive stress was calculated over the full velocity domain, averaged in time, then linearly interpolated to the swath centerlines. At each observed crevasse location, λ was calculated using the observed crevasse depth to ice thickness ratio and the LEFM-modeled crevasse depth was calculated as the maximum depth where K_I from Eq. (1) was greater than or equal to K_{IC}.

3 Results

3.1 Observed Crevasse Depths

We identified a total of 52644 crevasses in 381 elevation profiles among the 19 study glaciers (Enderlin, 2019). Broadly, crevasse occurrence increased towards each glacier terminus. Crevasse depth distributions are shown in Fig. 2 and depth profiles are shown in Fig. S4. We present statistics pertaining to crevasse depth and concentration, i.e., number of crevasses per kilometer, within 5 km of glacier termini in Table 1. Of all observed crevasses, the median depth was 6.2 m and median concentration was 17.2 crevasses per kilometer (one crevasse every 58 m). The crevasse concentrations span a fairly narrow range of values, with ~75% of crevasse concentrations between 15.0-19.7 crevasses km^{-1}, despite a wide range of glacier thicknesses and strain rates. The two relatively uncrevassed glaciers (concentrations less than 10 km^{-1}) have floating tongues and occur in the coldest, high latitude regions. The maximum observed depth of 64.9 m occurred at steep, fast-flowing Helheim Gletsjer. Helheim also had the deepest median crevasse depth of 10.2 m. While some glaciers have more and deeper crevasses near the terminus than inland, this pattern is clearly not universal, and in many instances, crevasse depths decreased over the last several km of the terminus region (Figs. 2, S4).

Although the crevasse size distributions are dominated by a large number of relatively shallow (i.e., <10 m-deep) crevasses, we are primarily interested in the deepest crevasses, which are the most likely to penetrate the full glacier thickness and therefore play an important role in iceberg calving and meltwater routing to the glacier bed. To isolate the deepest crevasses from the observations, we identified the maximum crevasse depth at 150 m-increments along flow so that the along-flow variations in crevasse depth had the same spatial resolution as the velocity data used to compute strain rates. To determine

whether along-flow variations in maximum crevasse depth can be explained by either local variations in local longitudinal strain rates or strain history (i.e., longitudinal strain rate integrated along flow), we normalized the crevasse depth, strain rate, and strain history data to facilitate direct comparison of their along-flow patterns. Data were linearly normalized such that the observed values span from zero to one. The normalized profiles in Fig. 3 suggest that along-flow variations in maximum crevasse depth cannot be simply explained as a function of variations in either local strain rate or strain history, although kilometer-scale variations in maximum crevasse depth at approximately half of the glaciers appear to follow patterns in strain history.

3.2 Crevasse Depth Comparison

At all spatial scales and over all time periods, the minimal model produced crevasse depths that were typically deeper than observed depths in extensional zones. This result could potentially arise from the fact that our observations are minimum estimates of crevasse depth, however, the observed-modeled depth discrepancy was not spatially consistent and the model failed to predict crevasses in compressional zones, as demonstrated for Inngia Isbræ in Fig. 4. Identical plots are shown for the other glaciers in the supplemental material (Figs. S5-S22). In Fig. 4 and Figs. S5-S22, where modeled and observed crevasses were in good agreement, the data fall along the 1:1 line separating the white and gray regions. Where crevasses were observed but strain rates were negative, i.e., crevasses were missed by the model, the data fall along the x-axis. Although the maximum misfit and occurrence of missed crevasses decreased at longer spatial scales, discrepancies between observed and modeled depths on the order of tens of meters were observed at all spatial scales.

The comparisons of observed and modeled crevasse depths in Fig. 4 and Figs. S5-S22 also suggest that crevasse depths remained relatively stable at all study glaciers over the 2011-2018 period. Inngia Isbræ exhibited the largest dynamic change among our study glaciers – the glacier retreated by ~4 km and thinned by ~100 m near the terminus (Fig. 4a) and flow accelerated by ~500 m/yr near the terminus (not shown) from 2012-2017 – yet crevasse depths do not significantly differ over time, and nearly all observed crevasse depths remain < 30 m throughout the observation record (Fig. 4b). The stable and consistent nature of the kilometers-scale oscillations in crevasse depth are also visible for each glacier in Fig. S4. Uncertainties are not included in Fig. S4, but a large portion of the observed variations in crevasse depth are within the observational uncertainty of ~3 m for the observed depths.

We illustrate spatial variations in the discrepancy between modeled and observed crevasse depths at four study sites – Kong Oscar (northwest Greenland), Inngia (west), Daugaard-Jensen (east), and Heimdal (southeast) – in Fig. 5. For each panel, we represent temporal variability in modeled depths (driven by strain rate changes) in a minimal model (Fig. 5, orange shading, see Methods), but finding no clear pattern in the temporal variability, only identify modeled depths computed from the median

speed profile for the remainder of our analysis (Fig. 5, colored lines). The complete set of plots, arranged geographically, are included in the supplemental material (Fig. S23).

Modifications of the minimal Nye model, including model variations with a threshold strain rate, different viscosities, and impounded water depth parameters reduced the overall discrepancy between the observations and models. However, even these more complex, tuned models could not accurately reproduce spatial patterns in crevassing. For example, one parameter with a clear physical motivation is the critical strain rate: because ice has tensile strength, crevasses will not form where the strain rates (and therefore tensile stresses) do not exceed an appropriate tensile strength-dependent threshold. We found that the addition of an observation-based non-zero critical strain rate does not improve agreement between observed and modeled crevasse depths (Fig. 5; red lines). Instead, there is an increase in the extent of modeled no-crevasse regions without compensatory improvements in the accuracy of crevasse depths elsewhere.

Along-flow variations in ice viscosity associated with strain-induced variations in crystal fabric or temperature, cryohydrologic warming, or even the presence of crevasses themselves may also contribute to along-flow discrepancies between the modeled and observed crevasse depths. Inclusion of a deformation enhancement parameterization that varies linearly along flow (Fig. S2) results in improved model performance in extensional zones (Figs. 5, S23; green lines). However, despite the expected along-flow increase in the deformation enhancement factor with damage, strain heating, etc., minimization of modeled/observed crevasse depth misfits (Eq. 4) reveals an along-flow *decrease* in deformation enhancement for approximately half of the glaciers (Fig. S2).

Increasing crevasse water depths, potentially associated with increasing melt at low elevations, represent another potentially important process, modifying the Nye minimal model, and adding another layer of complexity to the deformation enhancement approach. Using the inland-most deformation enhancement factor and tuning impounded water depths to minimize the observed-modeled depth misfit, we obtain first-order estimates of modeled crevasse water depths. Water depths necessary for this minimization vary from ≤3.2 m for Zachariae Isstrøm to ≤32.7 m for Kong Oscar Gletsjer (Table 1). Modeled crevasse depths obtained using parameterized water depths are shown in Figs. 5 and S21 (blue lines). Again, and as with the deformation enhancement factor, we find inconsistent, positive and negative trends in crevasse water depth with surface elevation. Approximately half of the glaciers displayed patterns of increasing water depth with decreasing surface elevation, as expected (Fig. S3). However, the remaining half of glaciers showed either decreasing or no change in estimated water depths at the low-elevation, near-terminus regions. Inclusion of a simple parameterization that scales crevasse water depth as a linear function of elevation improved the model's ability to capture kilometers-scale patterns in crevasse depth (Fig. S23) but could not explain the smaller-scale oscillations in crevasse depth that we observed. Inconsistent patterns of putative crevasse water depth lead us to suggest that this additional free model parameter is not reliably capturing the physics of the glacier crevassing.

In contrast to the Nye model, the LEFM model predicts realistic crevasse depths without the addition of model complexity, although in many cases, the spatial pattern of LEFM crevasses suffers the same deficiencies as the minimal Nye model and its variants. Excluding regions of longitudinal compression, where both the LEFM and Nye formulations fail to predict crevassing, the median depth for the minimal, $\dot{\varepsilon}_{crit}$ >0, damaged, and water-filled versions of the Nye formulation are 29 m, 16 m, 0 m, and 2 m greater than the maximum observed crevasse depths on average. On average, maximum LEFM depths are ~1 m deeper than the maximum observed depths under extension. However, like the Nye formulation, LEFM modeled crevasse depths are uncorrelated with observed crevasse depths, and the LEFM model fails to reproduce realistic along-flow variations in crevasse depth for most glaciers. Figures 5 and S21 show the maximum LEFM crevasse depths averaged over 300 m bins (purple). Purple shading indicates the effects of variations in the fracture toughness are obscured by the profiles for the intermediate fracture toughness value (K_{IC} =50kPa m$^{1/2}$).

4 Discussion and Conclusions

Using the first spatially and temporally extensive record of surface crevasse depths for Greenland's fast-flowing marine-terminating glaciers, we find that there are typically >10 crevasses per kilometer but that the majority of crevasses are <10 m in depth. Given the skewed distributions of crevasse depths in Fig. 2, the inclusion of crevasses smaller than our detection threshold of 3 m-depth would likely increase the concentration and decrease the median depths relative to those reported in Table 1. Crevasse depths are highly variable along flow, with pronounced changes in the shapes of the crevasse depth distributions and maximum crevasse depths evident at most glaciers (Figs. 2, 3). Although large-scale variations in maximum crevasse depth follow strain history at approximately half of our study sites (Fig. 3), small-scale patterns in crevasse depth cannot easily be explained by variations in local longitudinal strain rate, strain history, or stress.

The discrepancy between modeled and observed crevasse depths is problematic for numerical ice flow models that rely on spatio-temporal variations in crevasse depth to prescribe the terminus position. If calving is the result of crevasse penetration to the waterline, then the use of either the poorly-performing Nye or LEFM models in prognostic simulations is unlikely to reliably simulate glacier behavior. Furthermore, the predicted absence of crevasses in compressional zones could prevent modeled retreat, or lead to punctuated episodes of retreat and temporary stabilization, biasing projections of dynamic mass loss from marine-terminating glaciers.

Some of the physical processes present within the models tested here are undoubtedly important to true ice fracture, even if they are not predictive in the forms tested within this study. For example, ice is known to have tensile strength, and therefore there is likely some threshold strain rate or stress below which crevasses will not form (see van der Veen (1998)). Inclusion of a non-zero threshold strain rate for crevasse formation decreases the *average* misfit between the observed and Nye-modeled

crevasse depths from ~29 m to ~16 m but the misfit reduction is accompanied by a decrease in crevasse occurrence, even in places where they are observed. Thus, in the form presented here, the inclusion of a non-zero threshold strain rate for crevasse formation does not improve model performance. More realistic performance is found with the LEFM model, which, similar to the Nye model with $\dot{\varepsilon}_{crit}$ >0, assumes that crevassing occurs only where the longitudinal stresses exceed a critical threshold for crevasse initiation (i.e., stress concentration > fracture toughness). The LEFM-modeled depths are in much better agreement with observations in regions of longitudinal extension (~1 m misfit) and, since the LEFM model takes into account the full stress tensor (via the effective stress) rather than just the along-flow longitudinal stress, there are fewer crevassed regions where the LEFM model fails to predict crevassing.

The modeled depths that incorporate deformation enhancement are generally in better agreement with observations than with the minimal model and typically have similar magnitudes and spatial variations in crevasse depth as the LEFM model. This is not surprising since the deformation enhancement factor is calculated using a priori crevasse depth information, similar to the LEFM model. However, there is no clear physical explanation for the contrasting along-flow patterns in inferred enhancement, which suggest some glaciers have more viscous ice towards the terminus and others have less viscous (more ductile) ice towards the terminus. Although the LEFM model performance is similar for the Nye model with hydrofracture, the inferred water depths are problematic. There are few observations of hydrofracture in Greenland to which we can compare our inferred water depths, but the spatial patterns are unrealistic – they can vary by tens of meters over hundreds of meters along flow and do not follow expected regional patterns in meltwater runoff. Furthermore, approximately 1/4 of our observations were acquired prior to the onset of widespread seasonal surface melting. Because crevasses are known to drain over the course of the melt season (Everett et al., 2015; Lampkin and VanderBerg , 2014), we expect no water impounded in crevasses during spring. Therefore, even though model accuracy is improved by tuning, the optimal deformation enhancement and water depth tuning parameters found here have no physical basis and should not be used to improve model agreement with observations.

Based on the comparison of observed crevasse depths with local strain rates, strain history, and modeled crevasse depths, we hypothesize that our inability to reproduce small-scale (i.e., sub-kilometer) variations in observed crevasse depths using the Nye formulation stems from both its assumption of reduced stress concentration at crevasse tips in dense fields of crevasses and its ignorance of crevasse advection. As ice is advected into a stress field that favors crevasse formation, the depth to which a newly-formed crevasse penetrates depends on the instantaneous stress state as well as the micro- and macro-scale damage that the parcel of ice has inherited throughout its history (Bassis and Jacobs, 2013). If a crevasse penetrates deeper than its surrounding crevasses, then it will reduce the stresses on its neighbors, which will penetrate shallower than inherently assumed by the Nye formulation (van der Veen, 1998). Propagation is favored at the deepest crevasses as they advect through extensional flow regimes, as supported by the observed along-flow increase in maximum crevasse depths at over half of our glaciers. Focusing of stresses within individual, deep crevasses is also supported by the better performance of the LEFM formulation. The LEFM model uses the observed crevasse depth to ice thickness ratios to account for the depth-dependent

nature of stress concentration and crevasse propagation, with considerably improved performance relative to Nye model. When either model is informed by a priori knowledge of crevasse depths, many of the large-scale spatial patterns in crevasse depths can be reproduced, but the simplifying assumption that crevasse depth is a function of the local stress state still results in model failure in regions of longitudinal compression.

The inability of the existing, local stress-dependent formulations to simulate the complex patterns in observed crevasse depths for fast-flowing outlet glaciers is problematic for a number of reasons. Unrealistic spatial variations in modeled crevasse depths may result in undue emphasis on the role of surface crevassing as a control on recent and future changes in terminus position. However, our analysis of observed and modeled crevasse depths also suggests that advection of crevasses, and their associated mechanical and thermodynamic softening of ice, may exert an important control on the glacier stress balance. Confident projections of dynamic mass loss therefore require additional investigations on crevassing, including the impacts of spatio-temporal variations in crevassing on hydrologic routing, flow enhancement via damage and cryohydrologic warming, and iceberg calving. We anticipate that these findings will spur novel efforts to model crevasse evolution, as well as the parameterization of calving in numerical ice flow models.

Data Availability

The crevasse size distribution datasets constructed for this study are publicly archived at the Arctic Data Center (doi: 10.18739/A2WH2DF1F).

Author Contributions

EME formulated the study, developed the code for the analysis, performed the majority of the data extraction, compilation, and analysis, and wrote the initial draft of the manuscript. TCB provided guidance on methodology and revised the manuscript.

Acknowledgements

This project is funded by NSF Office of Polar Programs collaborative awards 1933105 and 1714639 to E.M. Enderlin and 1716865 to T.C. Bartholomaus. We would like to thank Editor Stef Lhermitte and the two anonymous reviewers for their recommended improvements to the analysis and its presentation in the manuscript.

Competing Interests

The authors declare that they have no conflict of interest.

References

Andreas, E.: Parameterizing scalar transfer over snow and Ice: A review, J. Hydrometeor., 3, 417–432, 2002.

Bassis, J. N. and Jacobs, S.: Diverse calving patterns linked to glacier geometry, Nat. Geosci., 6, 833-836, doi:10.1038/ngeo1887, 2013.

Benn, D. I., Warren, C. R. and Mottram, R. H.: Calving processes and the dynamics of calving glaciers, Earth-Sci. Rev., 82, 143-179, 2007a.

Benn, D. I., Hulton, N. R. J. and Mottram, R. H.: 'Calving laws', 'sliding laws' and the stability of tidewater glaciers, A. Glaciol., 46, 123-130, 2007b.

Bjork, A. A., Kruse, L. M. and Michaelsen, P. B.: Brief Communication: Getting Greenland's glaciers right – a new dataset of all official Greenlandic glacier names, The Cryo., 9, 2215-2218, doi:10.5194/tc-9-2215-2015, 2015.

Carr, J. R., Stokes, C. R. and Vieli, A.: Threefold increase in marine-terminating outlet glacier retreat rates across the Atlantic Arctic: 1992–2010, A. Glaciol., 58(74), 72–91, doi:10.1017/aog.2017.3, 2017.

Cathles, M., Abbot, D., Bassis, J. and MacAyeal, D.: Modeling surface-roughness/solar-ablation feedback: Application to small-scale surface channels and crevasses of the Greenland ice sheet, A. Glaciol., 52, 99–108, 2011.

Colgan, W., Rajaram, H., Abdalati, W., McCutchan, C., Mottram, R., Moussavi, M. S. and Grigsby, S.: Glacier crevasses: Observations, models, and mass balance implications, Rev.Geophys., 54, doi:10.1002/2015RG000504, 2016.

Colgan, W., Steffen, K., McLamb, W., Abdalati, W., Rajaram, H., Motyka, R., Phillips, T. and Anderson, R.: An increase in crevasse extent, West Greenland: Hydrologic implications, Geophy. Res. Lett., 38, L18502, doi:10.1029/2011GL048491, 2011.

Cook, S., Zwinger, T., Rutt, I. C., O'Neel, S. and Murray, T.: Testing the effect of water in crevasses on a physically based calving model, A. Glaciol., 53, 90–96, 2012.

Cook, S., Rutt, I. C., Murray, T., Luckman, A., Zwinger, T., Selmes, N., Goldsack, A. and James, T. D.: Modelling environmental influences on calving at Helheim Glacier in eastern Greenland, The Cryo., 8, 827-841, doi: 10.5194/tc-8-827-2014, 2014.

Enderlin, E.: Elevation profile-derived crevasse depths for select Greenland marine-terminating glaciers, 2011-2018, Arctic Data Center, doi:10.18739/A2WH2DF1F, 2019.

Everett, A., Murray, T., Selmes, N., Rutt, I. C., Luckman, A., James., T. D., Clason, C., O'Leary, M., Karunarathna, H., Moloney, V. and Reeve, D. E.: Annual down-glacier drainage of lakes and water-filled crevasses at Helheim Glacier, southeast Greenland, J. Geophys. Res.: Earth Surface, 121(10), 1819-1833, 2016.

Hock, R.: Glacier melt: A review of processes and their modelling, Prog. Phys. Geog., 29, 362–391, 2005.

Howat, I.M. and Eddy, A.: Multi-decadal retreat of Greenland's marine-terminating glaciers, J. Glaciol., 57(203), 389-396, 2011.

Lampkin, D. J., and VanderBerg, J.: Supraglacial melt channel networks in the Jakobshavn Isbræ region during the 2007 melt season, Hydro. Proc., 28(25), 6038-6053, 2014.

Moon, T.K. and Joughin, I.: Retreat and advance of Greenland tidewater glaciers from 1992 to 2007, J. Geophys. Res., 113, F02022, doi:10.1029/2007JF000927, 2008.

Mottram R. H. and Benn, D. I.: Testing crevasse-depth models: a field study at Breiðamerkurjökull, Iceland, J. Glaciol., 55(192), 746-752, 2009.

Nick, F. M., Vieli, A., Anderson, M. L., Joughin, I., Payne, A., Edwards, T. L., Pattyn, F. and van de Wal, R. S. W.: Future sea-level rise from Greenland's main outlet glaciers in a warming climate, Nature, 497, 235–238, doi:10.1038/nature12068, 2013.

Noh, M. -J. and Howat, I. M.: Automated stereo-photogrammetric DEM generation at high latitudes: Surface Extraction with TIN-based Search-space Minimization (SETSM) validation and demonstration over glaciated regions, GIS. Rem. Sens., doi:10.1080/15481603.2015.1008621, 2015.

Nye, J.F.: The distribution of stress and velocity in glaciers and ice sheets, Proc. Roy. Soc. London. Series A, 239, 113–133, 1957.

Otero, J., Navarro, F. J., Lapazaran, J. L., Welty, E., Puczko, D. and Finkelnburg, R.: Modeling the controls on the front position of a tidewater glacier in Svalbard, Front. Earth Sci., 5, 29, doi:10.3389/feart.2017.00029, 2017.

Pfeffer, W. and Bretherton, C.: The effect of crevasses on the solar heating of a glacier surface, Int. Assoc. Hydro. Sci. Pub.s: The Physical Basis of Ice Sheet Modelling 170, 191–205, 1987.

Pollard, D., DeConto, R. M. and Alley, R. B.: Potential Antarctic Ice Sheet retreat driven by hydrofracturing and ice cliff failure, Earth Planet. Sci. Lett., 412, 112-121, doi: 10.1016/j.epsl.2014.12.035, 2015.

Poinar, K., Joughin, I., Lilien, D., Brucker, L., Kehrl, L. and Nowicki, S.: Drainage of Southeast Greenland firn aquifer water through crevasses to the bed, Front. Earth Sci., 5, 5, doi:10.3389/feart.2017.00005, 2017.

Reese, R., Gudmundsson, G. H., Levermann, A. and Winkelmann, R.: The far reach of ice-shelf thinning in Antarctica, Nature Clim. Change, 8, 53-57, doi: 10.1038/s41558-017-0020-x, 2018.

Rott, H., Skvarca, P. and Nagler, T.: Rapid collapse of northern Larsen Ice Shelf, Ant. Sci., 271, 788–792, 1996.

Scambos, T. A., Hulbe, C., Fahnestock, M. and Bohlander, J.: The link between climate warming and break-up of ice shelves in the Antarctic Peninsula, J. Glaciol., 46, 516–530, doi:10.3189/172756500781833043, 2000.

Scambos, T. A., Fricker, H. A., Liu, C. -C., Bohlander, J., Fastook, J., Sargent, A., Massom, R. and Wu, A.-M.: Ice shelf disintegration by plate bending and hydro-fracture: Satellite observations and model results of the 2008 Wilkins ice shelf break- ups, Earth Planet. Sci. Lett., 280, 51–60, doi:10.1016/j.epsl.2008.12.027, 2009.

Stevens, L. A., Behn, M. D., McGuire, J. J., Das, S. B., Joughin, I., Herring, T., Shean, D. E. and King, M. A.: Greenland supraglacial lake drainages triggered by hydrologically induced basal slip, Nature, 522, 73-76, 2015.

Trantow, T. and Herzfeld, U.C.: Crevasses as Indicators of Surge Dynamics in the Bering Bagley Glacier System, Alaska: Numerical Experiments and Comparison to Image Data Analysis, J. Geophys. Res.: Earth Surf., 123(8), 1615-1637, doi:10.1029/2017JF004341, 2018.

Van der Veen, C. J.: Fracture mechanics approach to penetration of surface crevasses on glaciers, Cold Reg. Sci. Technol., 27(1), 31–47, 1998.

Vieli, A. and Nick, F. M.: Understanding and modeling rapid dynamic changes of tidewater outlet glaciers: Issues and implications, Surv. Geophys., 32, 437–458, doi:10.1007/s10712-011-9132-4, 2011.

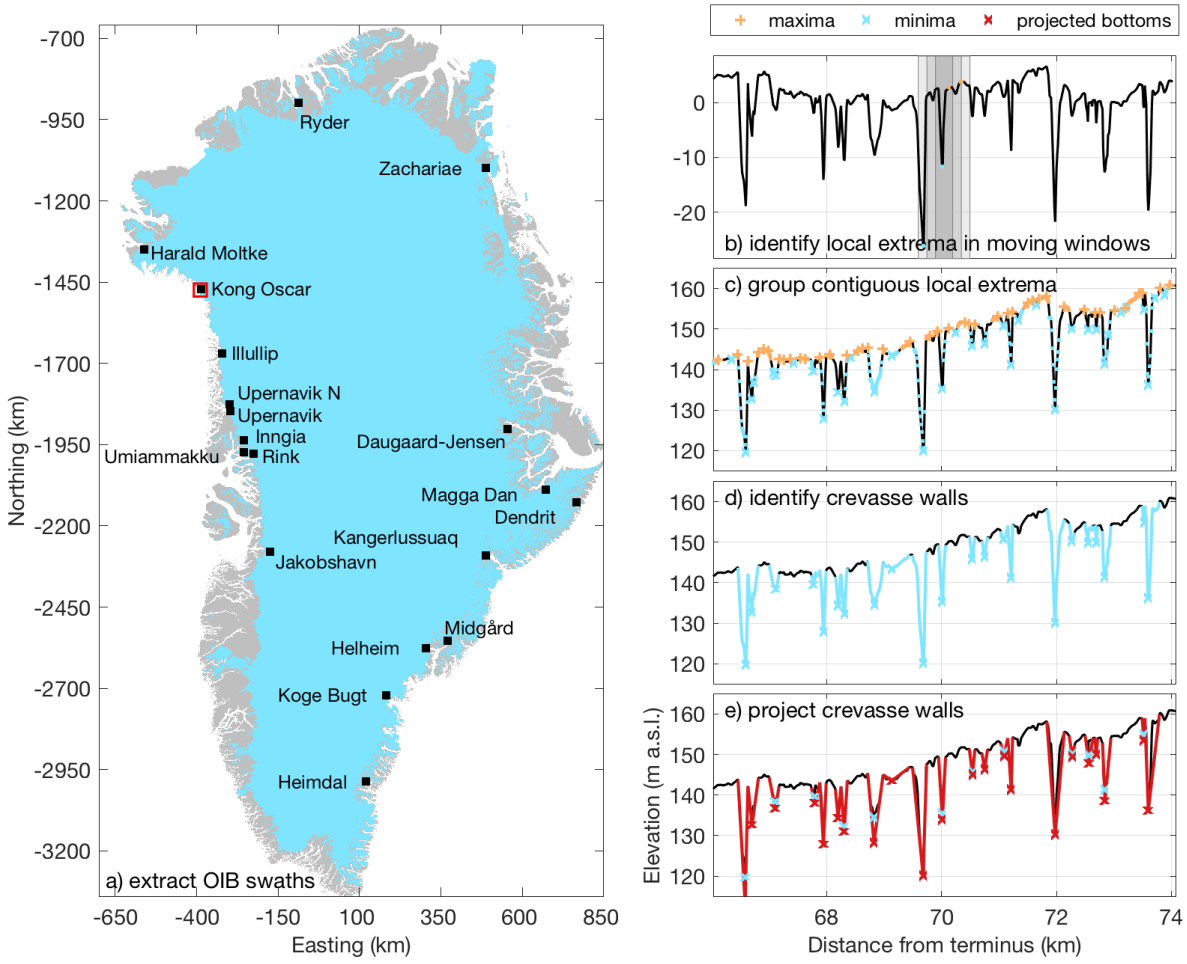

Figure 1: Map of glacier locations and example of the crevasse depth estimation approach applied to the elevation data for each glacier. a) Operation IceBridge transects (black squares) overlain on the Greenland Ice Mapping Project ice mask (light blue) and land mask (gray). Glacier names are from Bjork et al. (2015). The red box highlights the location of the profile in panels b-e. b) Moving window approach to find local extrema. The nested search windows (gray shading) and local extrema (colored points) overlain on the de-trended portion of the profile. Local extrema were filtered to c) isolate crevasse bottoms (blue x's) and top edges (orange +'s), d) locate steeply-sloped crevasse walls (blue lines), and e) project wall slopes to depth.

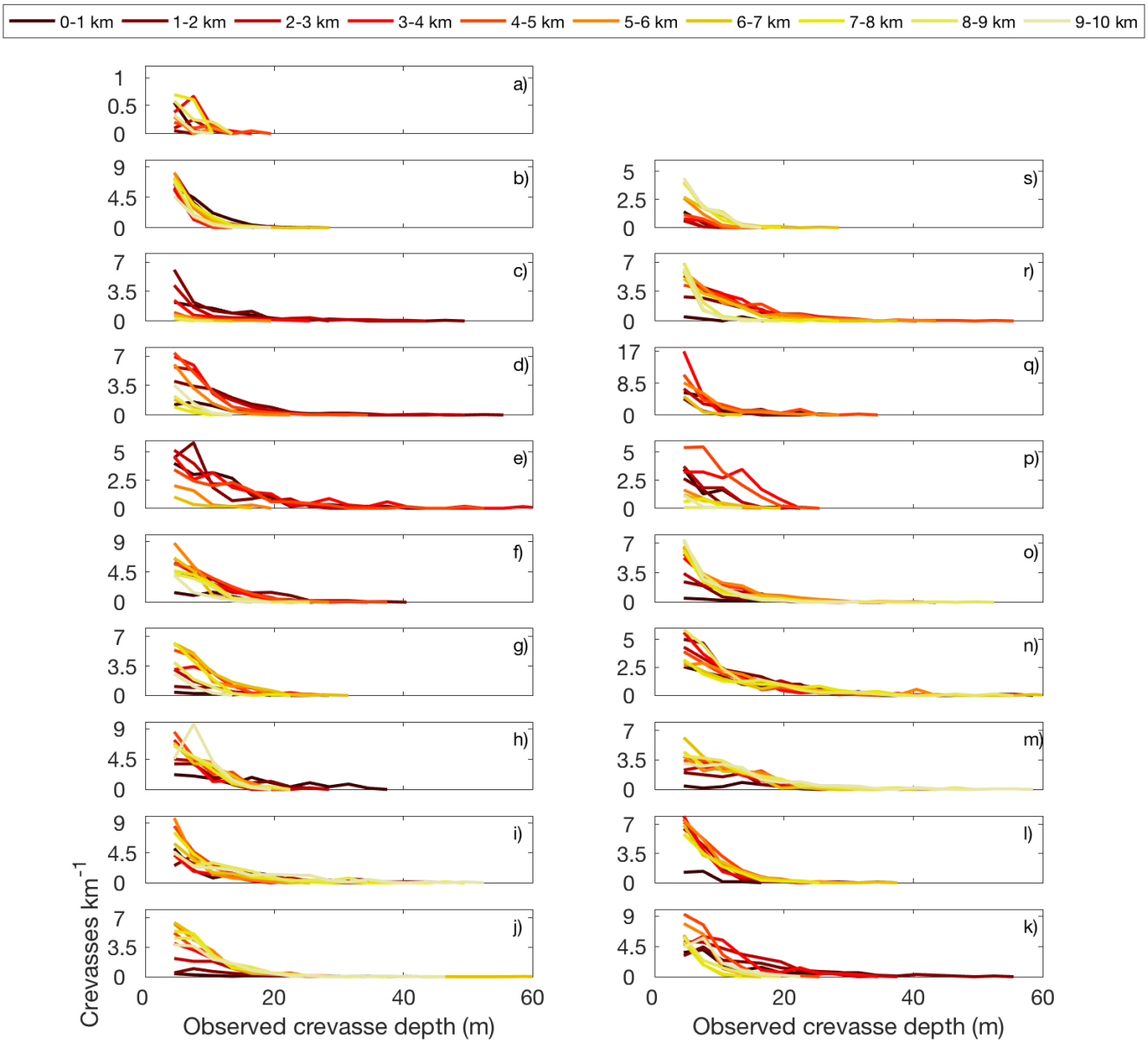

505 **Figure 2: Observed crevasse depth distributions for 1km-wide bins over the first 10km of each glacier. The distance from the terminus of each bin is distinguished by line color. Differences in area under the curves reflect variations in observed crevasse concentration between bins. Panels are geographically arranged so that western glaciers are on the left and eastern glaciers are on the right. Common names (Greenlandic names) are a) Ryder Gletsjer, b) Harald Moltke Bræ (Ullip Sermia), c) Kong Oscar Gletsjer (Nuussuup Sermia), d) Illiup Sermia, e) Upernavik North Isstrøm, f) Upernavik Isstrøm (Sermeq), g) Inngia Isbræ (Salliarutsip**
510 **Sermia), h) Umiammakku Sermiat, i) Rink Isbræ (Kangilliup Sermia), j) Jakobshavn Isbræ (Sermeq Kujalleq), k) Heimdal Gletsjer, l) Koge Bugt Gletsjer, m) Helheim Gletsjer, n) Midgård Gletsjer, o) Kangerlussuaq Gletsjer, p) Dendrit Gletsjer, q) Magga Dan Gletsjer, r) Daugaard-Jensen Gletsjer, s) Zachariae Isstrøm.**

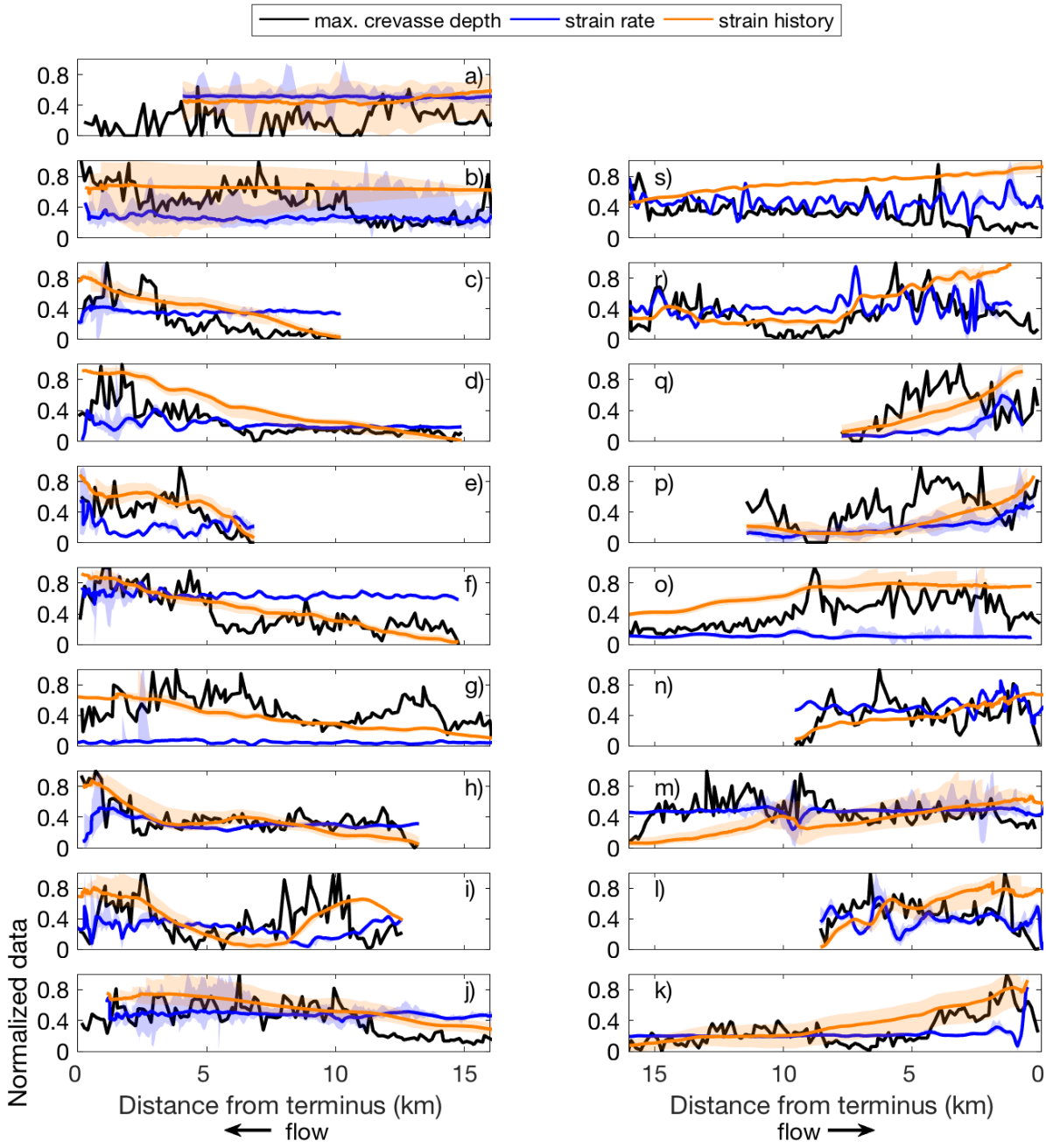

515 **Figure 3: Normalized profiles of maximum crevasse depth, local strain rate, and strain history. In each panel, the maximum crevasse depth in 150 m-wide bins is in black, the local strain rate is in blue, and the strain history is in orange. The median strain rate and strain history are shown as lines with shading indicating their temporal ranges. As in Fig. 2, the panels are geographically arranged.**

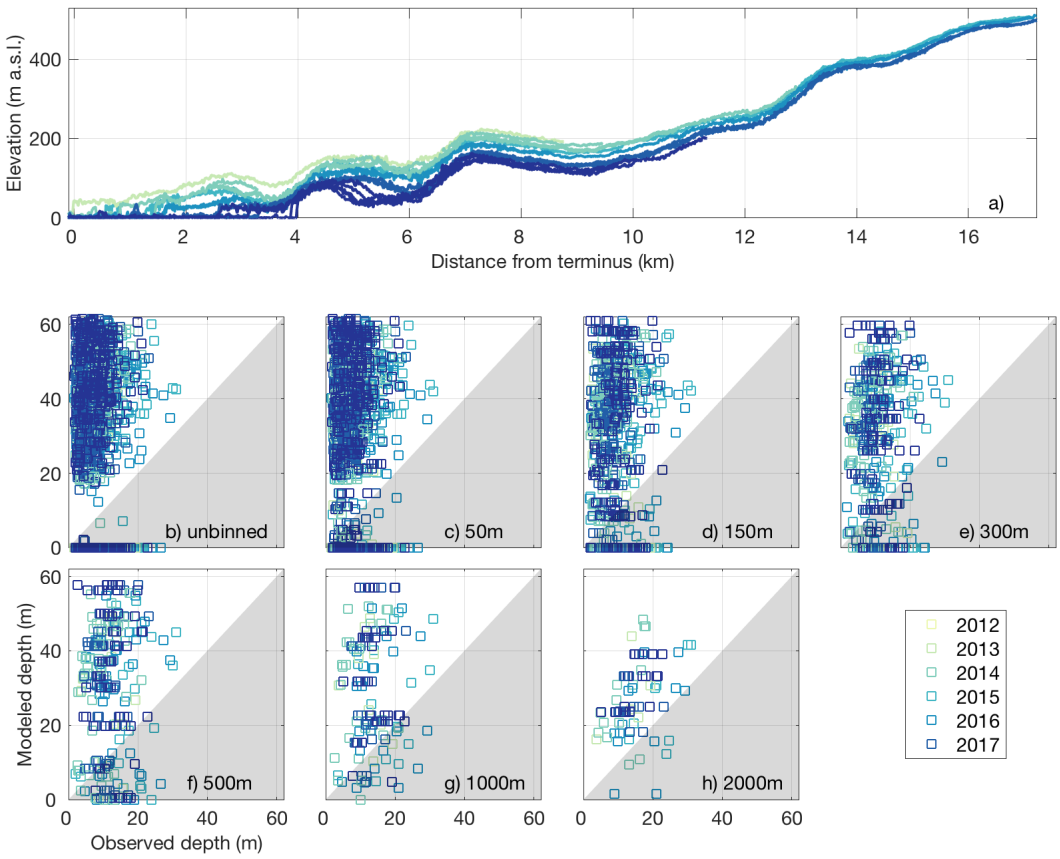

Figure 4: Inngia Isbræ (Greenlandic Name: Salliarutsip Sermia) crevasse depth data. The legend indicates the observation year for all panels. a) Elevation profile time series extracted along the OIB swath. b-h) Scatterplots of observed crevasse depths plotted against modeled crevasse depths. Points that fall in the white (gray) region represent model over-estimates (under-estimates) of observed depths. All observations are shown in b whereas the maximum observed and median modeled depths within along-flow bins are shown in c-h. The bin sizes in c-h (50-2000 m) reflect the range of spatial resolutions for numerical ice flow models.

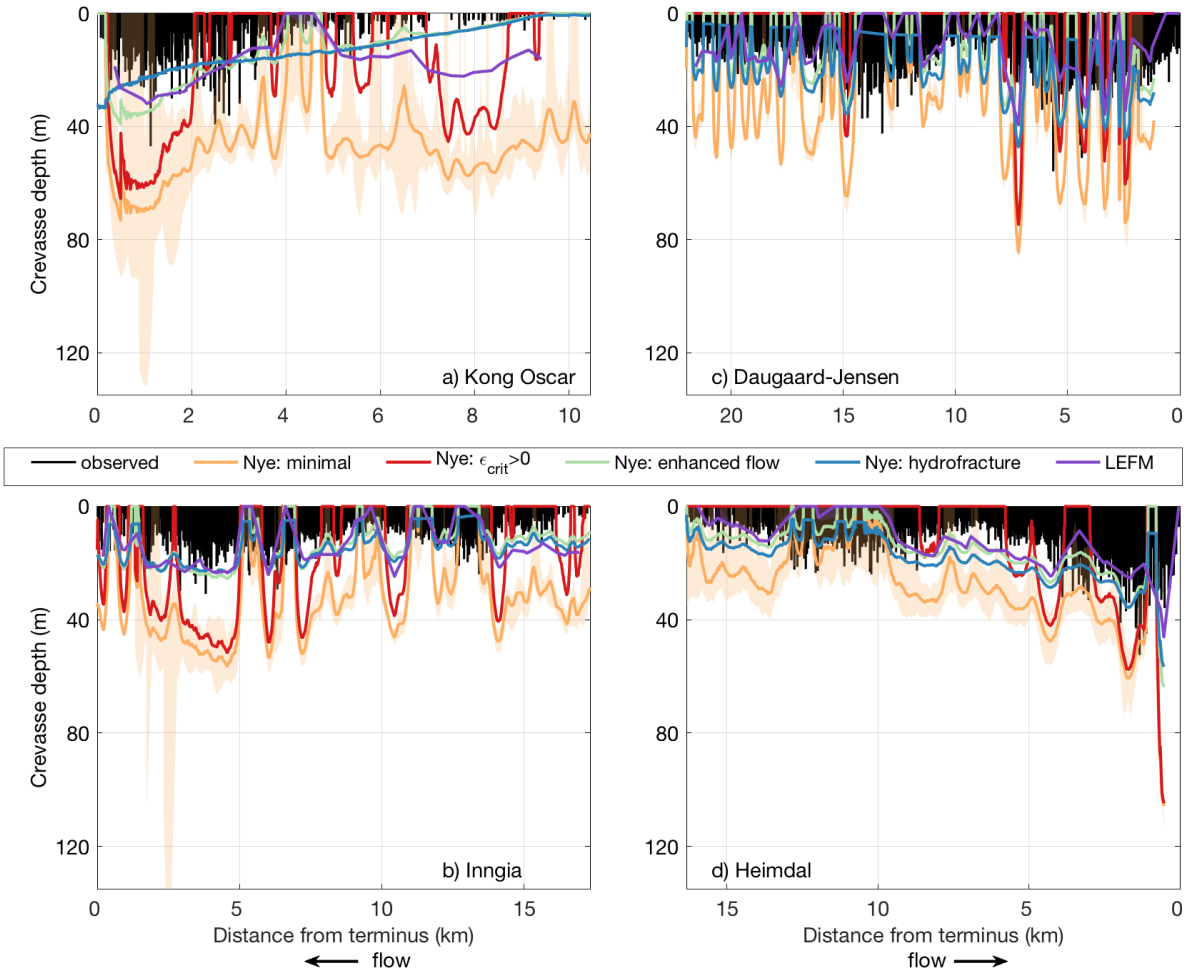

Figure 5: Profiles of all observed crevasse depths (black lines) and modeled crevasse depths (colored lines) computed from the median velocity profile for a) Kong Oscar Gletsjer, b) Inngia Isbræ, c) Daugaard-Jensen Gletsjer, and d) Heimdal Gletsjer. Orange colors show the median (line) and temporal range (shading) in modeled crevasse depths using the minimal Nye formation (i.e., no critical strain rate, uniform viscosity, no water). The red, green, and blue lines show the Nye-modeled crevasse depths with observation-based critical strain rates, flow enhancement, and flow enhancement with impounded water, respectively. The purple lines show the LEFM-modeled crevasse depths with the geometry-dependent stress intensity scaling factor calculated from observations.

Glacier Name	Latitude (°N)	Longitude (°E)	Max. Observed Depth (m)	Median Observed Depth (m)	Concentration (crevasses/km)	Max. Nye Depth (m)	Median Nye Depth (m)	Deformation Enhancement (unitless)	Max. Water Depth (m)	Max. LEFM Depth (m)	Median LEFM Depth (m)
Ryder	81.7802	-50.4556	10.9	4.8	1.0	29.4	15.2	0.64	6.1	5.1	5.1
Harald Moltke	76.5718	-67.5659	21.1	3.3	15.2	34.8	22.2	0.63	10.2	11.9	9.7
Kong Oscar	76.0267	-59.7052	47.0	5.0	9.6	69.7	46.6	0.79	*32.7*	28.7	23.1
Illullip	74.4026	-55.9341	46.6	6.3	16.9	90.8	62.9	0.77	*25.0*	43.4	31.9
Upernavik North	72.9511	-54.1183	59.9	8.6	17.8	118.5	52.2	0.70	*30.7*	56.3	40.4
Upernavik	72.8461	-54.1578	36.3	7.6	19.6	69.6	41.4	0.58	*10.8*	33.8	20.8
Inngia	72.1022	-52.5047	29.3	6.2	17.2	56.4	33.8	0.64	6.4	24.1	19.8
Umiammakku	71.7685	-52.3880	35.3	6.9	15.2	64.7	39.1	0.55	9.4	32.0	28.9
Rink	71.7381	-51.6096	31.6	5.9	21.9	72.3	49.7	0.62	13.1	34.3	23.5
Jakobshavn	69.1166	-49.4560	58.6	7.3	17.9	72.3	61.9	0.67	28.1	34.7	24.6
Heimdal	62.8969	-42.6730	24.0	5.4	18.5	33.8	28.2	0.58	12.7	18.8	14.9
Koge Bugt	65.2097	-41.2156	35.1	5.9	17.3	106.3	58.2	0.76	8.7	41.0	27.1
Helheim	66.3941	-38.3800	64.9	10.2	15.0	51.5	37.1	0.38	5.8	11.9	8.0
Midgård	66.5119	-36.7300	55.4	9.3	19.0	108.2	56.8	0.54	14.0	33.2	21.8
Kangerlussuaq	68.5864	-32.8397	50.0	4.5	17.8	80.8	45.9	0.70	*27.9*	40.4	18.6
Dendrit	69.3449	-25.1687	23.9	6.5	11.4	52.8	35.2	0.62	*7.3*	21.3	13.2
Magga Dan	69.9375	-27.1410	33.1	5.3	18.6	76.2	49.4	0.72	4.0	53.4	25.6
Daugaard-Jensen	71.8797	-28.6788	55.9	7.2	16.2	84.5	38.1	0.53	12.0	35.8	24.2
Zachariæ	78.9161	-21.0828	19.1	5.3	6.8	84.5	47.3	0.77	3.2	34.6	25.3

535

Table 1: Observed and modeled crevasse characteristics within 5 km of the terminus. The name, location, maximum and median observed crevasse depths, median concentration of crevasses, maximum and median Nye-modeled crevasse depths, median tuned deformation enhancement factor, maximum tuned water depth, and maximum and median LEFM-modeled crevasse depths for each study site.